Contents

List of Papers

I "Isomer spectroscopy of neutron rich $^{190}W_{116}$",
Zs. Podolyàk, P.H. Regan, M. Pfützner, J. Gerl, M. Hellström, M. Caamaño, P. Mayet, Ch. Schlegel, A. Aprahamian, J. Benlliure, A.M. Bruce, P.A. Butler, D. Cortina Gil, D.M. Cullen, J. Döring, T. Enqvist, F. Rejmund, C. Fox, J. Garcés Narro, H. Geissel, W. Gelletly, J. Giovinazzo, M. Górska, H. Grawe, R. Grzywacz, A. Kleinböhl, W. Korten, M. Lewitowicz, R. Lucas, H. Mach, M. Mineva, C.D. O'Leary, F. De Oliveira, C.J. Pearson, M. Rejmund, M. Sawicka, H. Schaffner, K. Schmidt, Ch. Theisen, P.M. Walker, D.D. Warner, C. Wheldon, H.J. Wollersheim, S.C. Wooding, and F.R. Xu,
Phys. Lett. B **491**, (2000) 225.

II "Isomer Spectroscopy of Fragmentation and Fission Products",
M.N. Mineva, M. Hellström, M. Bernas, J.Gerl, H. Grawe, M. Pfützner, Zs. Podolyák, P. H. Regan, and the GSI Isomer Collaboration,
Proc. 2nd International Balkan School on Nuclear Physics, Bodrum, Turkey, September 2000, submitted to Balkan Physics Letters.

III "A new μs isomer in ^{136}Sb produced in projectile fission of ^{238}U",
M.N. Mineva, M. Hellström, M. Bernas, J. Gerl, H. Grawe, M. Pfützner, P.H. Regan, M. Rejmund, D. Rudolph, F. Becker, C.R. Bingham, T. Enqvist, B. Fogelberg, H. Gausemel, H. Geissel, J. Genevey, M. Górska, R. Grzywacz, K. Hauschild, Z. Janas, I. Kojouharov, Y. Kopatch, A. Korgul, W. Korten, J. Kurcewicz, M. Lewitowicz, R. Lucas, H. Mach, S. Mandal, P. Mayet, C. Mazzocchi, J.A. Pinston, Zs. Podolyàk, H. Schaffner, Ch. Schlegel, K. Schmidt, K. Sümmerer, and H.J. Wollersheim,
submitted to EPJ A.

Chapter 1

Introduction

Nuclei far from stability have been an interesting and exciting field for both theoretical and experimental studies for decades. Figure 1.1 shows the Segré map of nuclides in which the most important objects of interest in this work can be identified. The line of β-stability consists of about 270 isotopes, which in their ground state are stable against nuclear-decay modes. More than 2000 unstable isotopes from the proton- and neutron-rich side of the β-stability line have been studied, inspiring developments of both experimental tools and theoretical models. For example, the nuclear shell structure along the β-stability line has been well studied, but the shell structure in drip-line nuclei (i.e. nuclei for which the particle separation energy is equal to zero) is still unknown, and hence it is of great interest. An idea for existence of islands of stability was expressed some decades ago and people have always been trying to reach more and more "exotic" nuclear systems in terms of either synthesis of super-heavy elements, or producing nuclei with large excess or deficiency of neutrons towards the nuclear drip lines. During years of research questions arise such as: What is the shell structure for nuclei far from the β-stability line? Are the magic numbers there still the same? Do our models still work and how good can they interpret the experimental observables?

In Figure 1.1 ^{78}Ni, ^{132}Sn, and ^{208}Pb nuclei are marked. They are doubly magic nuclei, and are well bound, hence spherical in their ground states. They play an important role in the nuclear structure research. Studying nuclei in their close neighborhood, which have only a few valence particles or holes outside the closed shells, is an efficient probe into the general features of the nuclear many-body systems. For example, one may test the particle-hole or proton-neutron interactions, the particle-core polarization and excitation modes, nuclear deformations. It is convenient to compare the different sets of doubly magic nuclei and their surrounding nuclei in order to explore the change in nuclear structure when different orbitals are occupied and different shells are filled. It has been shown that some similarities exist between the ^{208}Pb and ^{132}Sn regions. Blomqvist [1] and later Leander *et al.* [2] have shown that every (n, l, j) single-particle state in the ^{132}Sn region has a $(n, l+1, j+1)$ counterpart in the ^{208}Pb region, with corresponding ordering and energy spacing. Omtvedt *et al.* [3] provide experimental data which prove that the residual interactions and the quadrupole properties of the two regions are rather similar. The $E2$

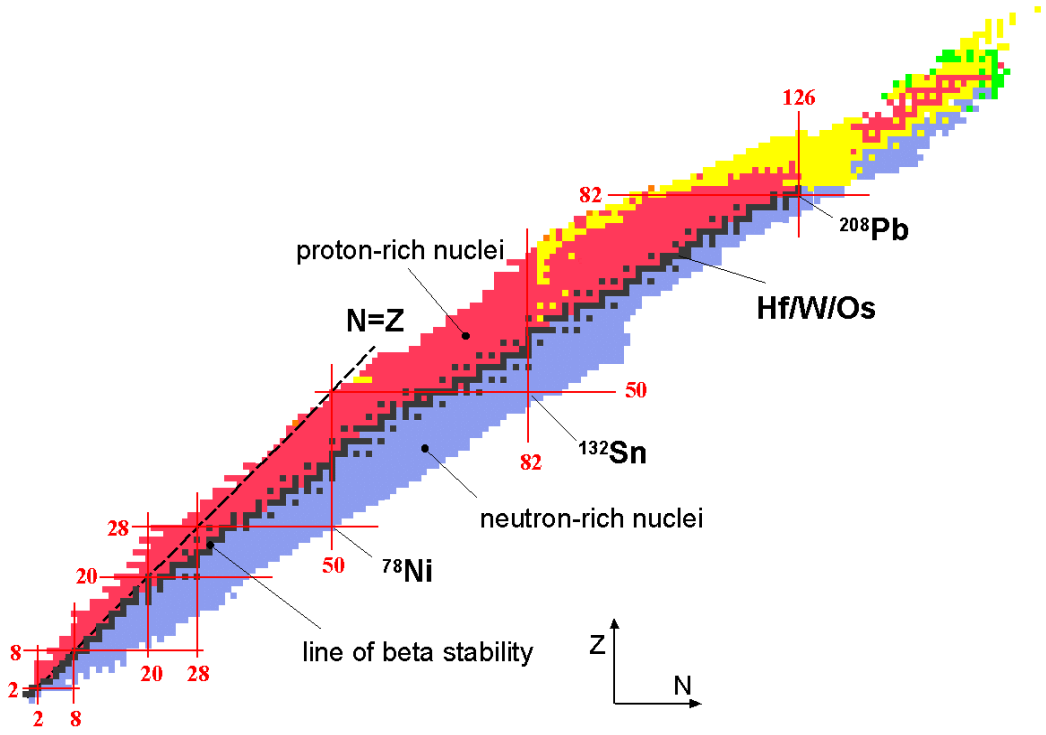

Figure 1.1: The Segré map of the nuclides.

effective charges are essentially equal. However, the negative-parity collective states in ^{132}Sn are much higher in excitation energy than in ^{208}Pb. Thus, the octupole properties of the two regions may differ significantly.

^{208}Pb is the heaviest doubly magic nuclear system which could be studied so far. It is a stable, and the most abundant Pb isotope. ^{78}Ni and ^{132}Sn are lighter systems, but their experimental study is more difficult because of their larger neutron excess. This is illustrated In Figure 1.2. ^{132}Sn has eight neutrons in addition to its heaviest stable isotope ^{124}Sn. The situation is even more difficult for ^{78}Ni, where this number is 14. The neutron-separation energy drops with the neutron excess, and this implies technical difficulties in the production of neutron-rich nuclei. Recently, with the development of the radioactive nuclear beams (RNB) it became possible to explore more and more exotic nuclei far from the line of beta stability produced in relativistic heavy ion reactions [4, 5]. The experimental study of isomeric states in the ^{132}Sn region applying RNBs forms the major part of this licentiate work. In addition, so-called K-isomers (see Sec. 2.2) have been investigated.

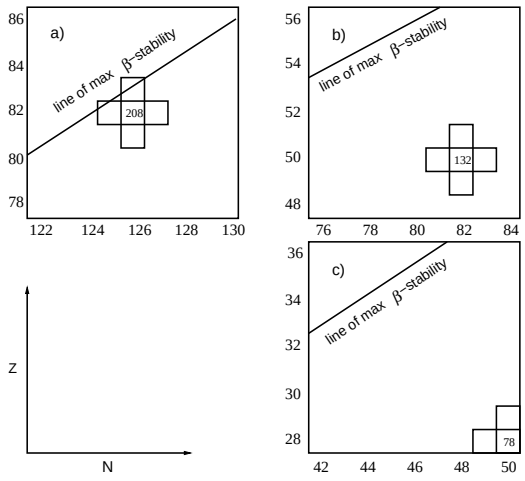

Figure 1.2: Comparison of the location of the three doubly magic nuclei ^{208}Pb (a), ^{132}Sn (b), and ^{78}Ni (c) relative to the line of β-stability. The large neutron excess of ^{132}Sn and ^{78}Ni implies experimental difficulties due to low production cross sections.

Chapter 2

Physics of the neutron-rich nuclei and theoretical predictions

Let us focus on the very neutron-rich side of the nuclidic chart, which is the subject of the present study. The neutron-drip line is experimentally known only from hydrogen ($Z = 1$) up to oxygen ($Z = 8$). In the neutron-rich isotopes of the light nuclides the so-called halo phenomenon exists. The halo is formed by the loosely bound neutrons surrounding the core. The weak binding allows to distribute nuclear matter in regions not allowed classically. Thus halo nuclei are characterized by very large radii. Secondly, they are very diffuse and their properties are greatly dominated by surface effects. Halo phenomena are the subject of study of many experimental and theoretical groups.

In heavier neutron-rich systems the weak neutron binding implies the existence of a 'neutron skin' (i.e., a dramatic excess of neutrons at large distances). The existence of a neutron skin may lead to new vibrational modes in which, for example, the neutron skin oscillates out of phase with a well-bound proton-neutron core [6]. In those nuclei we can have the opportunity to study in the laboratory nearly pure neutron matter.

With increasing the neutron number other effects start to play a role due to the decreasing neutron separation energy. Mean field calculations of the spherical single-particle levels by Dobaczewski *et al.* [7], using Hartree-Fock (HF) and Hartree-Fock-Bogoliubov (HFB) models with Skyrme-type SkP interactions, predict a dramatic decrease of the $N = 82$ shell gap near the neutron-drip line. A quenching of the shell effects at the neutron-drip line is expected only in the systems with $N \leq 82$. Later calculations by Werner *et al.* [8] predict the $N = 82$ shell gap to be considerably reduced for $Z = 46$. Weakening of shell effects with neutron number manifests itself in the behavior of two-neutron separation energies. On the other hand HFB calculations with other standard Skyrme-force parameterizations such as SIII and SkM [9] show strong shell closures. Possible explanation of this fact is the low effective mass in these forces [10]. Thus different models have different predictions not only about the shell quenching but also about the location of the neutron-drip line.

2.1 The ^{132}Sn region

The stiffness of the doubly-magic core of ^{132}Sn has been discussed in [1, 11]. The core excitation of ^{132}Sn itself is studied in details and it is very well known. A summary of the current experimental information is done in the work by Fogelberg *et al.* [12], and no new experimental information has been added recently. The first excited state in ^{132}Sn is at 4.0 MeV, which suggests that the single-particle states in the surrounding nuclei should be rather pure. The simplest excitations in doubly-magic and in the neighboring nuclei are particle-hole excitations. The p-h states of these nuclei form level multiplets where the individual states often have a very simple structure with regards to admixture of configurations. The mapping and identification of such multiplets may give immediate information on the nuclear two-body matrix elements and single-particle energies, which are crucial elements in any theoretical model. Almost all single particle (hole) energies in the region have been measured as summarized by Grawe and Lewitowicz [13]. A number of empirical two-particle, two-hole, and particle-hole multiplets have been identified as well. The coupling of valence particles and holes often gives rise to isomeric states with moderate spin and with lifetimes in the microsecond regime. This offers a good possibility for spectroscopy of the decay of the γ-cascade below the isomer.

Now it is interesting to extend the knowledge to more neutron-rich nuclei and nuclei with more valence particles outside the doubly-magic core to investigate the onset of deformation and development of collectivity. A challenging experiment is the systematic study of the $N = 82$ isotones below $Z = 50$ towards the nuclei for which the shell quenching was predicted. Unfortunately, as already stated earlier the more exotic the system is, the more difficult the experiment is.

2.2 K-isomers in the Hf/W/Os region

In the $A \approx 170 - 190$ rare-earth nuclei a specific type of isomerism occurs, originating from valence particles occupying high-j orbitals with a large projection Ω_j of the angular momentum on the nuclear symmetry axis. These nuclei are axially symmetric. Therefore, the collective rotation R takes place about the short axis, perpendicular to the symmetry axis, and the collective angular momentum is thus zero along the symmetry axis. The coupling of the single-particle angular momenta is shown in Fig. 2.1. The projection of the total angular momentum on the symmetry axis is $I_3 = K + R = K$, where K is built by the single particle momenta Ω_j, $K = \sum_j \Omega_j$, and is a constant of motion (i.e. it is a good quantum number characterizing the system). The decay of such a high-K states to low-K rotational states is often hindered due to the large difference ΔK. The only way such high-K states can decay is via large alternation of the orientation of the total angular momentum, which is forbidden via low multipolarity transitions if the K projection is a good quantum number. Thus, such states become long-lived, i.e. isomeric. The hindrance factor grows exponentially with the degree of K-forbiddenness, $\Delta K - \lambda$ [14], where λ is the multipolarity of the transition.

The observation of isomeric decay by K forbidden transitions implies that there must be some mixing of K values. Suggestions for the mechanism of "K-mixing" include Coriolis mixing, and γ-deformation tunneling [15]. Coriolis mixing arises because a rotating nucleus is not an inertial frame of reference, and the orientation of a nucleon's orbit is modified by the rotation of the nucleus. The γ-tunneling involves shape fluctuations where the deformation of the nucleus changes from prolate shape ($\gamma = -120°$) to prolate shape ($\gamma = 0°$) through the intermediate oblate ($\gamma = -60°$) shape.

K-mixing raises the question of the limits of K-forbiddenness and the limits of the K-isomerism. It has been predicted that this region will extend into the neutron-rich Hf/W/Os region with $A \approx 180 - 200$ [16, 17]. These nuclei are expected to be triaxially deformed (i.e. the size of the nucleus along all three axis is different), and the isomers are expected to have shorter lifetimes.

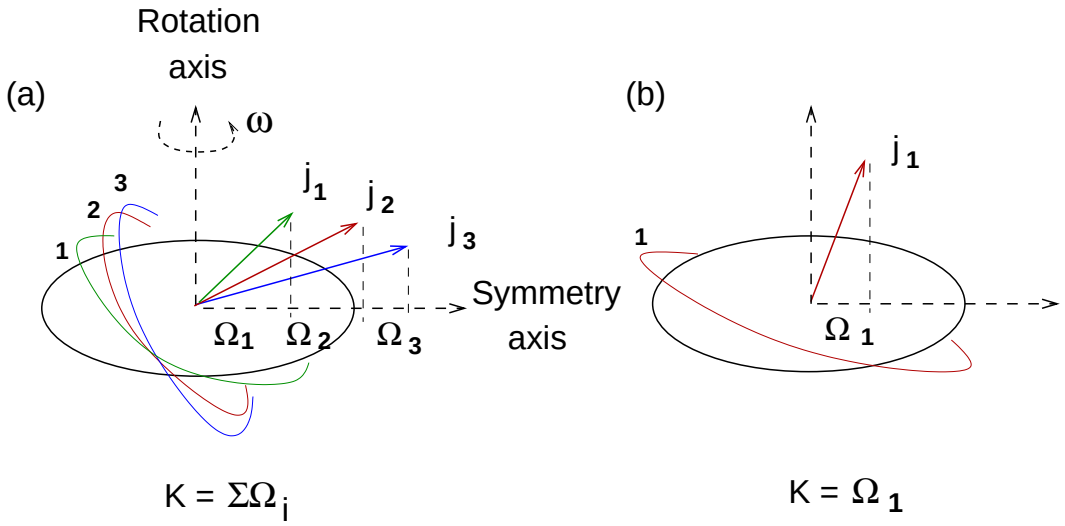

Figure 2.1: K-isomerism is a characteristic feature of deformed nuclei with axial symmetry (a). The collective angular momentum along the symmetry axis is zero, and the projection of the total angular momentum I is built by the sum of the projections of the single particle momenta j_i. Decay to a lower K state (b) requires rearrangement of nucleons and a change in the orientation of the angular momentum relative to the axis of symmetry.

Chapter 3

Experimental technique

Depending on which part of the nuclidic chart and what parameters of the nuclei one wants to study, different production mechanisms can be applied. For the spectroscopy of proton-rich and stable nuclei the most suitable method is a heavy-ion fusion evaporation reaction. In this reaction nuclei are produced in excited states with relatively high angular momenta and excitation energies [18]. In projectile fragmentation the maximum yields and production cross sections are along the β-stability line, but this type of reaction populates also proton-rich as well as neutron-rich nuclei. Nuclear fission is the most suitable method for producing neutron-rich nuclei. This work is focused on γ-ray spectroscopy of isomer decays of neutron-rich nuclei, produced in projectile fragmentation and in-flight fission. The following two sections of the chapter will give more detailed explanation of the two production mechanisms.

3.1 Projectile fragmentation

When a heavy projectile, accelerated to energies much above the Coulomb barrier, interacts with a target nucleus, the probability for a fragmentation reaction is very high. Depending on the actual energy of the bombarding ions and on the impact parameter, several different regimes are possible. At low energies ($E/u < 20$ MeV/nucleon) there are several mechanisms contributing to the reaction, including Coulomb scattering, incomplete fusion, and fusion evaporation reaction [19]. Reactions occurring at much higher energies ($E/u > 200$ MeV/nucleon) are considered to be "pure" fragmentation [20]. In this energy regime depending on the impact parameter we can have projectile fragmentation in the case of peripheral collisions, and multifragmentation takes place in the case of a central collisions. The "pure" projectile fragmentation is a two step process as discussed in [20].

Figure 3.1 shows a schematic view of the two-step reaction. In the peripheral collisions between the bombarding heavy ion and the target nucleus, the nucleons in the overlapping area ("participants") become very hot and excited nuclear matter, which is almost immediately abraded off. This is a very fast process which occurs within 10^{-21}s. The remaining part of the projectile ("spectator") undergoes statistical evaporation (also known as "ablation") of particles and light clusters, after which

we observe the final products of the reaction. This step takes about 10^{-16} s. The momenta (or velocity) of the final products is very similar to those of the projectile. Due to the high energy involved in the collision we can have a rather extensive range of the mass of the final observed products. Therefore it is suitable for spectroscopy of both proton- and neutron-rich nuclei.

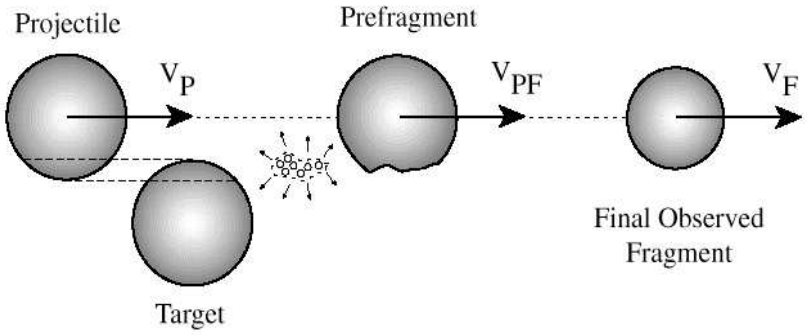

Figure 3.1: Projectile fragmentation at relativistic energies ($E > 200$ MeV/u, $\beta > 0.7$). The final observed fragment has momentum very similar to the one of the projectile.

3.2 In-flight fission

The best method to produce (very) neutron-rich nuclei is nuclear fission. In this work the so-called in-flight or projectile fission of heavy-ions at relativistic energies has been used. In this reaction the heavy ion (for example ^{238}U) is accelerated to relativistic energy. The target nucleus can be light (e.g. ^{9}Be) or heavy (e.g. ^{208}Pb), inducing fission by peripheral nuclear interactions for the U/Be system, or by dissociation in the electro-magnetic field for the U/Pb system [21].

The projectile splits into two relatively cold fragments, which are emitted in opposite directions from each other in the reference system of the fissioning nucleus (Figure 3.2). The products are isotropically distributed in a sphere. In the laboratory frame the distribution transforms into a narrow cone centered in the beam direction. The process is shown schematically in Figure 3.3. The velocity of the fission fragments in the laboratory frame is the relativistic addition of projectile and fission velocities β_0 and β_F. Thus, the forward flying fragments get an additional 'kick' in momentum. In that sense the projectile fission is an exothermal reaction for the products distributed in the forward semi-sphere with respect to the beam direction. The relativistic character of the process has a great advantage compared to the fission at rest. It allows the use of spectrometer for extraction of a secondary beam as explained in section 3.3, and identification of the reaction products event

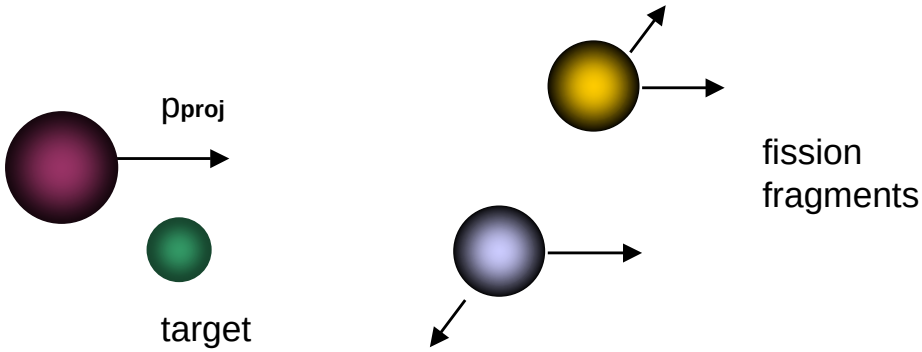

Figure 3.2: Projectile fission at relativistic energies ($E > 500$ MeV/u, $\beta > 0.8$). The two fission fragments are relatively cold, and are emitted in a forward and backward direction in the reference system of the projectile.

by event, as discussed in sect. 4.1. Unfortunately, due to the limited acceptance of the spectrometer, not all reaction products can be transmitted and studied simultaneously. The opening angle of the cone is about ±30 mrad, and the acceptance angle of the spectrometer is ±15 mrad.

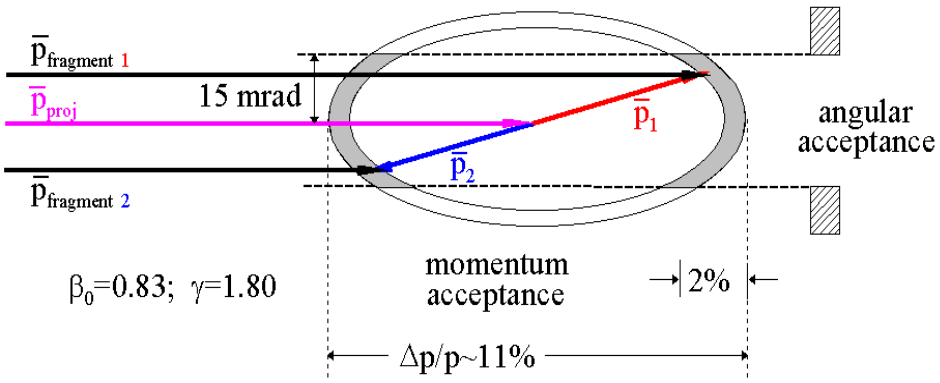

Figure 3.3: Momentum distribution of the relativistic fission fragments in the laboratory system. The part of the distribution accepted by the separator is indicated by the filled areas.

In his Ph.D. thesis Engelmann [22] investigates the reaction kinematics and shows that there is a gain factor with respect to the fission at rest: the high velocity of the fissioning projectile nucleus (≈ 83% of the speed of light for a primary beam with $E = 750$ MeV/u) leads to an optimal transmission for those fragments, flying in

either forward or backward direction with respect to the beam. This means that for equal fission rates one can observe nuclei produced with cross sections up to three orders of magnitude smaller than the one we can observe with fission at rest.

3.3 Separation of the reaction products - the FRS

In both types of production mechanism described above up to 10^3 different isotopes are created in the target due to the high energy involved in the reaction. To separate only the ions which we are interested in (to obtain a pure secondary radioactive beam which then can be studied), we use a tool called the FRagment Separator (FRS). It is an achromatic magnetic forward spectrometer [23]. Heavy-ion beams with magnetic rigidities from 5 to 18 Tm can be analyzed by the device. Figure 3.4 shows the main parts of which the FRS consists. There are four 30 deg dipole magnets determining four independent stages of the spectrometer and a number of quadrupole and sextupole magnets providing variable magnetic fields up to 1.6 Tesla. The quadrupole magnets before each dipole are designed to achieve a high resolving power by properly illuminating the field volume of the bending magnets. The ion-optical conditions at the four focal planes S1 to S4 are determined by the quadrupoles following each dipole. The function of the sextupole magnets placed in front of and behind each dipole is to provide correction for second-order abberations. A secondary-electron detector (SEETRAM) placed upstream of the first target station measures the beam intensities [24]. In the target area and at each focal plane, two-dimensional grids with gas amplification and current readout are used for beam alignment and count rate measurements. The particle detection is performed by using multi-wire proportional chambers [25] installed at all of the focal planes. Pairs of these detectors are used for particle tracking to analyze the primary beam or secondary radioactive beam with respect to position, angle, and $B\rho$ value. The reaction takes place in the target, ions are selected by their mass to charge ratio A/q in the first stage of the separator. In this first step about 10^2 different reaction products are selected. The separation is based on magnetic analysis combined with energy losses in matter ($B\rho - \Delta E - B\rho$ method). Energy degraders with variable thicknesses are placed at the different focal planes of the separator. To introduce different energy loss for the fragments with different momenta a special wedge-shaped degrader is placed at the central focal plane S2. The different atomic energy loss of the ions penetrating the degrader provides an additional selection criterion. The best spatial separation can be obtained with a degrader shape which preserves the achromatism of the spectrometer. In this way at the final focal plane S4 we obtain a pure secondary beam consisting of the ion for which the separator was tuned and 10-15 neighboring isotopes. This will be called "production setting" and the fragment for which the separator has been tuned is referred to as the "setting fragment".

Secondary beams prepared by the FRS can be transferred to other experimental areas for performing different measurements. For the purpose of isomer γ-ray spectroscopy the beam is stopped at the final focal plane of the spectrometer and the

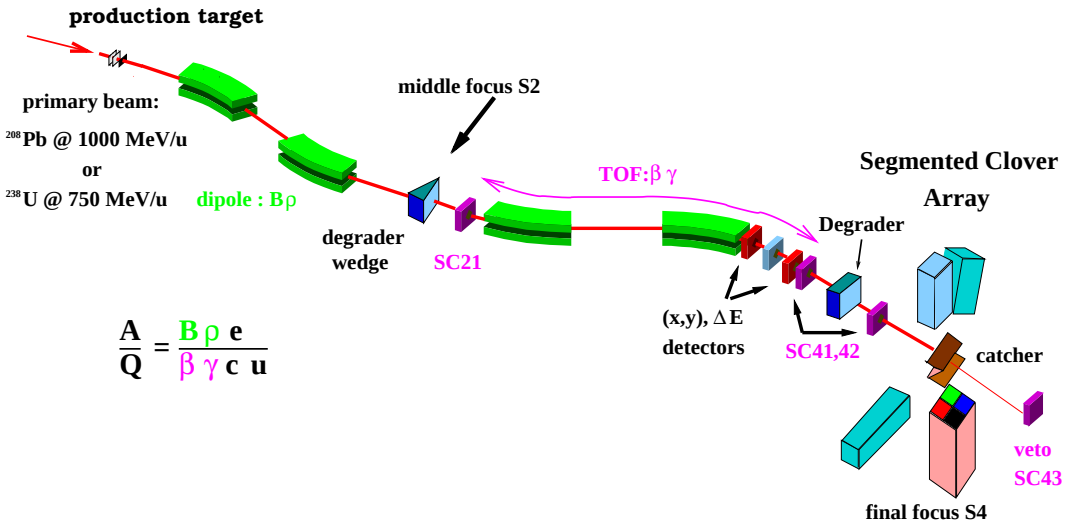

Figure 3.4: Schematic view of the FRagment Separator at GSI. After production in a target, the ions of interest are selected and separated with the help of the spectrometer. The flight path is 76 m. After passing various detector and degrader systems the selected products are brought to the final focal plane where delayed γ-ray spectroscopy can be performed.

products of interest are implanted in an aluminum catcher (Fig 3.4 and Fig. 3.5). In both experiments (see Table 3.1) the catcher was surrounded by four segmented germanium detectors of clover type [26], in which delayed γ-rays emitted by the implanted ions were detected. γ-rays from the decay of any isomeric state were recorded within a 80μs time gate, which was started with the detection of a heavy ion. The flight path of the ions trough the separator is about 300 to 400 ns, which typically sets a lower limit of about 100 ns for the lifetimes which can be studied, but exceptions have been observed (section 4.4.2). By using both TDCs and TACs, the timing information from the γ-rays was recorded in 0 to 8 μs and 0 to 80 μs ranges.

For a detailed preparation of an experiment at the FRS a Monte Carlo code (MOCADI, [27]) is used to simulate the optics, and the atomic and nuclear interaction processes including scattering and secondary reactions. In order to plan the stopping of the secondary beam the energy losses in matter (degraders, detectors, air) are calculated with the code ATIMA. The physics processes implemented in the program are discussed in Ref. [28]. Copper slits can be used to mechanically reduce the beam count rate if it is necessary, or to prevent the penetration of the primary beam through the separator.

To calibrate all detectors involved in the identification procedure a set of measurements with the primary beam through the separator at low intensity and with different energies is done before each production run. This procedure has another purpose as well, namely to fine-tune the separator and the ion optics by monitoring the centering of the beam and the angle of the beam at each focal point. This is

monitored by a system of current grids, plus multi-wire position-sensitive detectors measuring the beam position at the points of interest.

Figure 3.5: Photo of the final focal plane of the separator. The aluminum Z-shaped catcher of thickness 4-6 mm is surrounded by Ge clover detectors.

3.4 Experiments

The thesis is based on two experiments performed at the FRagment Separator (FRS) at GSI, Darmstadt using the technique described above. In April 1999 we used projectile-fragmentation of ^{208}Pb at 1 GeV/u to produce neutron-rich K-isomers. In December 1999 we studied neutron-rich nuclei in the ^{132}Sn region produced in projectile-fission of ^{238}U at the energy of 750 MeV/u. Table 3.1 summarizes some technical details about the experiments.

Table 3.1: Technical data about the experiments

Beam	Energy	Target	Reaction	Isomer search in
^{208}Pb	1000 MeV/u	1.6 g/cm^2 ^{9}Be	projectile fragmentation	n-rich Hf/Os/W
^{238}U	750 MeV/u	1.0 g/cm^2 ^{9}Be	projectile fission	vicinity of ^{132}Sn

Chapter 4

Analysis and results

4.1 Identification of the reaction products

The identification of the reaction products is done in the second stage of the separator. It is based on measurements of time-of-flight and energy loss, combined with information from position-sensitive detectors and the magnetic fields of the separator dipole magnets.

The time-of-flight (TOF) of the fragments is measured with plastic scintillators SC21 and SC41, placed at the middle focal plane after the S2 degrader, and at the final focal plane S4 after the vacuum window of the last magnet (cf. Figure 3.4). Normally the position tracking is done with the multi-wire proportional counters, but the scintillators can be used for position measurements in the horizontal direction as well. The position information from the scintillators is obtained from the time difference between signals from the left and right readout of the detector.

The velocity v of each ion is calculated from the TOF and the flight path. Position tracking is very important not only for the purpose of using the spatial separation of the ions, but to achieve the proper geometrical corrections to the TOF - respectively velocity, and to the magnetic rigidity of the second stage, $B\rho_2$. The $B\rho_2$ can be calculated from the expression:

$$B\rho_2 = B\rho_0(1 - \tfrac{x_4 - V_2 x_2}{D_2}) \ , \tag{4.1.1}$$

where $B\rho_0$ is the magnetic rigidity of particles at the ion-optical axis. V_2 and D_2 are properties of the ion optics of the FRS second stage, namely magnification and dispersion. x_2 and x_4 are the positions of the ion in the x-direction at the intermediate and the final focal planes respectively.

Combining the velocity and $B\rho_2$ information we can define the mass-to-charge ratio A/q for each fragment via the expression:

$$A/q = \tfrac{e}{uc}\tfrac{B\rho_2}{\beta\gamma} \ , \tag{4.1.2}$$

where e is the elementary charge, u is the atomic mass unit, $\beta = v/c$ is the ratio of the velocity of the ion to the speed of light, and γ is the Lorentz factor

($\gamma = 1/\sqrt{1-\beta^2}$). The proton number Z of each ion can be estimated under the assumption:

$$\Delta E = Z^2 f(\beta), \tag{4.1.3}$$

where the energy loss ΔE is measured in a MUltiple-Sampling Ionization Chamber (MUSIC) [29]. The function f which depends on the ion velocity is deduced from the primary beam calibration measurements. Figure 4.1 shows the ΔE spectrum measured during the ^{131}Sn production setting from the ^{238}U fission experiment. When analyzing only the fully stripped ions (i.e., ions which did not change their charge state) the following relation is valid:

$$\frac{A}{q} = \frac{A}{Z}, \tag{4.1.4}$$

With the help of this information particle identification in terms of A, Z, and position is achieved on an event-by-event basis for each ion. In addition, we have data from which we can estimate the transmission losses, a problem which is discussed in the following Section 4.2. In Figures 4.2 and 4.3 examples of identification maps are given.

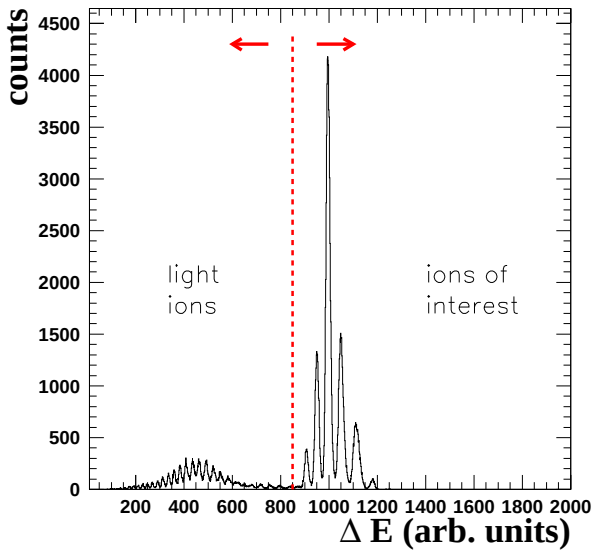

Figure 4.1: Energy loss measurement in the MUSIC detector for all fragments reaching the final focal plane of the separator in the ^{134}Sn setting (^{238}U fission experiment). A small fraction of light fission fragments is also being transmitted but later excluded in the analysis.

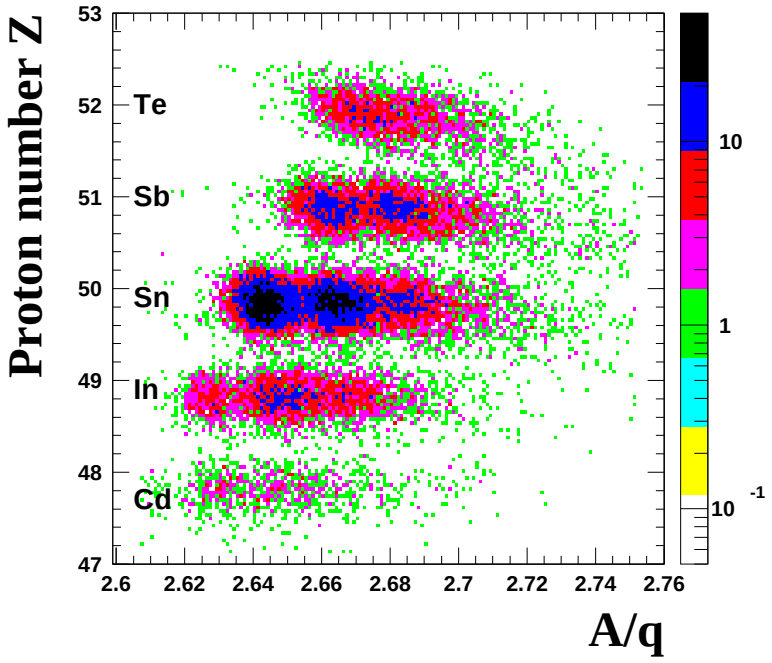

Figure 4.2: Identification plot from the ^{134}Sn setting in the ^{238}U fission run. The proton number Z is plotted versus the mass-to-charge ratio A/q for fragments reaching the final focal plane of the separator during the setting for ^{134}Sn. Each group represents a different isotope. For each Z several isotopes can be identified.

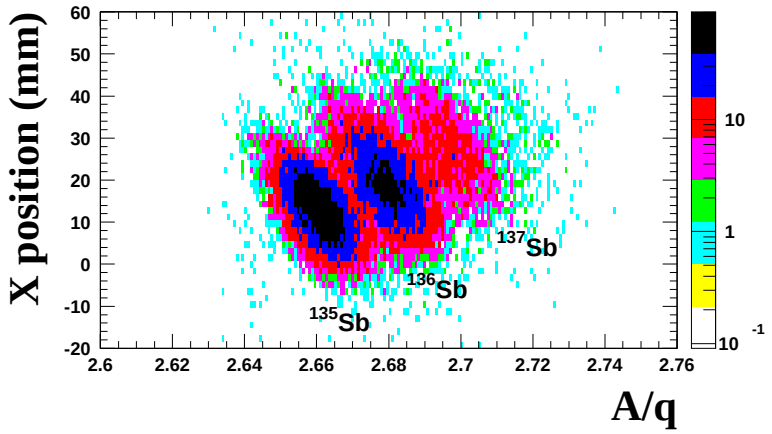

Figure 4.3: Events from the same setting as in Fig. 4.2 with Z selection, presented in different coordinates. The X position of the fragments at the final focus is plotted versus the mass to charge ratio A/q. The Z=50 group is selected and better mass separation is achieved.

4.2 Transmission and losses

There are several factors which affect the transmission of the reaction products through the separator. First of all, one should distinguish the term *optical transmis-*

sion, T_{opt}, from the *total transmission,* T_{tot}. The first is a measure of the efficiency of the ion-optics to transmit and focus the beam without losing particles in the process. The total transmission includes additional processes such as nuclear absorption, changes of charge states, and secondary reactions. The total transmission through the separator is typically $\approx 50\%$ for fragmentation and $\approx 2\%$ for fission products. The second process has a much lower transmission due to the specific kinematics of the in-flight fission reaction (Chapter 3.2).

When passing different materials, or already in the target, some products may change their charge state q. Thus we can transmit simultaneously fully stripped, H-like, and He-like charge states of the ions. To reduce the number of the fragments which change q by picking up an electron, a niobium stripping foil can be placed after the target, and after each degrader. This problem is especially important for heavy fragments ($Z > 50$), as in the case of the K-isomer study. This could lead to misidentification. However, there are methods to solve this problem. Ions which have changed their charge state cannot be spatially separated from the ones which have kept their charge state, but can be separated in the A/q space in the second stage of the spectrometer. In Figure 4.4 the separation of the different groups is illustrated. Three groups of ions can be clearly seen in (a) - those which have not changed their charge state ($\Delta q = 0$), those which have changed it with one unit ($\Delta q = 1$), and with two units ($\Delta q = 2$). The first group predominantly corresponds

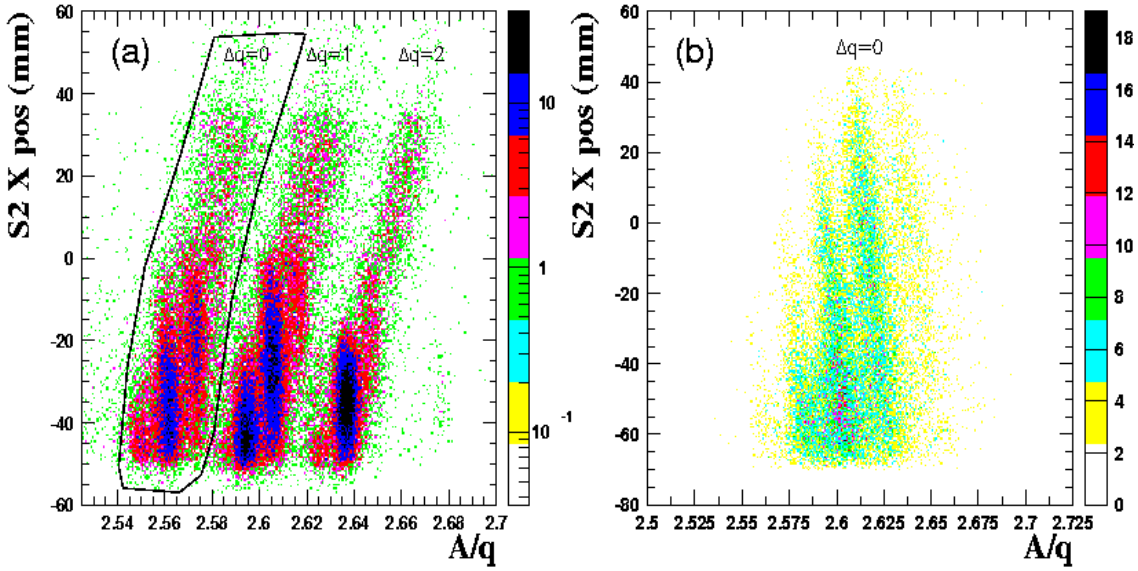

Figure 4.4: All fragments reaching the central focal plane of the separator. The events which have changed their charge state can be separated in the A/q space. Plot (a) is from $^{191}_{74}$W production setting in the ^{208}Pb fragmentation run, and plot (b) represents all fragments from the $^{131}_{50}$Sn setting during the ^{238}U fission experiment.

to fully stripped ions, to some extent contaminated by some H-like ions and with negligible contribution from He-like ions. The second group consists mainly of ions

which have picked up an electron at the intermediate focus. In Figure 4.4 panel (b) can be seen that this problem was completely negligible for lighter Z products. Indeed, 99% of the Sn ions were fully stripped from production to the final vacuum window of the spectrometer. The program GLOBAL [30], developed at GSI, can be used to calculate the charge states of the primary and secondary beams. Its capability to simulate the real processes has been tested and excellent agreement between the calculated and measured values has been found [31].

Additional losses in transmission are caused by secondary reactions of the fragments in the materials, especially in the thick S4 adjustable degrader. It is situated after the identification set-up and, therefore, there is a danger that fragments which have been identified as 'good fragments' are destroyed before being implanted, but still set a trigger for γ-detection. Therefore we are using a pair of plastic scintillators placed before and after the S4 degrader to compare the energy released by the fragments in the detectors before and after passing the degrader, and suppress 'bad' events (up to 30% for a given isotope). This is illustrated in Figure 4.5.

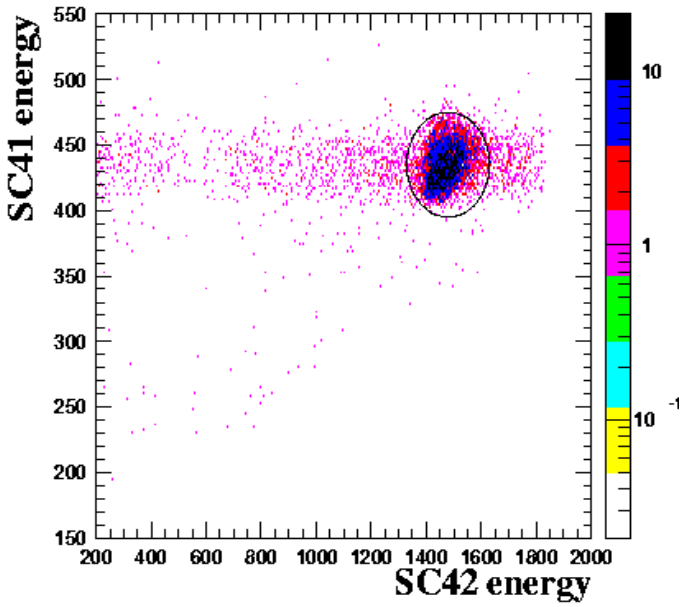

Figure 4.5: Energy loss in SC41 and SC42 scintillator detectors (cf Fig. 3.4) in arbitrary units. Only ^{136}Sb ions are selected. The group indicated by the ellipse represents ions which have not been destroyed in the S4 degrader.

4.3 Delayed γ-ray spectroscopy

A specific part of this experimental method is the slowing down and stopping of the secondary beam in the process of implanting in the aluminum catcher. This problem is widely being discussed currently in connection with the new projects taking place at the GSI facility - namely the "Stopped Beam" part of the RISING project [32].

The velocity of the products after the target is $\approx$ 80% of the speed of light. In the second stage of the FRS after the S2 degrader v/c is still $\approx$ 0.75. In order to implant the products of interest in the aluminum catcher we use an adjustable degrader at the S4 final focal plane for slowing down the ions which is typically 5-7 g/cm^2 aluminum. The interactions of the heavy ions with the degrader material causes a prompt burst of X-rays and low energy bremsstrahlung coming together with the heavy ion. Due to the prompt "flash" the effective γ-detection efficiency is reduced. This effect, which is highly dependent on the Z of the heavy ion, is under investigation but can be quite significant.

A big advantage of the method is the tagging of γ-rays with a specific ion which strongly reduces the background and makes possible studies of very weak channels ($<$ 100 ions per day). In addition this method is very convenient in search for new isomers, because during the flight through the separator all the prompt transitions have decayed. If one plots the matrix of the energy of the detected γ-rays from a particular isotope versus the time of their detection (Fig. 4.6), one can clearly see the pattern of the isomeric transition. The advantage of *isomer spectroscopy* is that the spectra can be "cleaned" by requiring the detection of delayed γ-rays associated with a given heavy ion. This is illustrated in Figure 4.7. All examples are from the ^{238}U fission experiment.

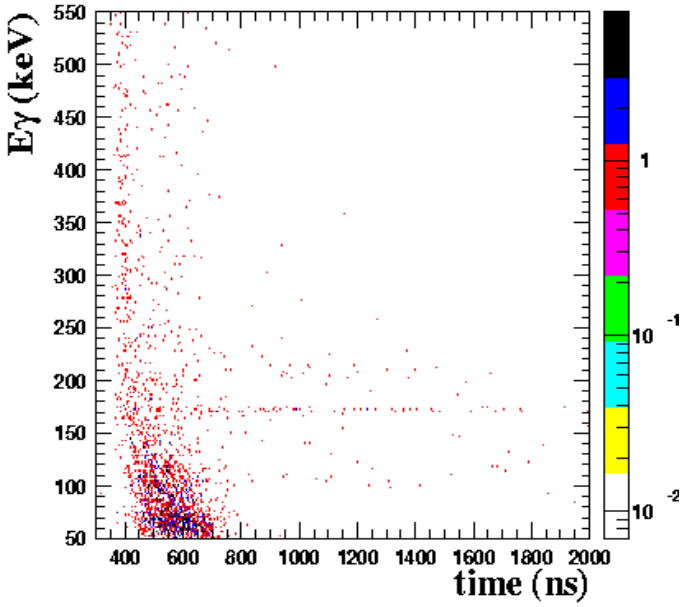

Figure 4.6: Energy-time matrix from one of the Clover detectors gated by ^{136}Sb ions identified in the FRS. The delayed pattern of the 173 keV isomeric transition is clearly seen.

If one makes a cut in the time-energy matrix (cf. Fig. 4.6) around a given peak and projects on the time axis the half-life of the corresponding transition can be measured. In Figure 4.8 two examples are presented. According to a criterion in Ref. [33], page 252, if the slope of the measured time spectrum is 1.5-2.0 times the

prompt slope, then simple slope fitting gives an accurate result. The results are summarized in Table 1 in Paper III.

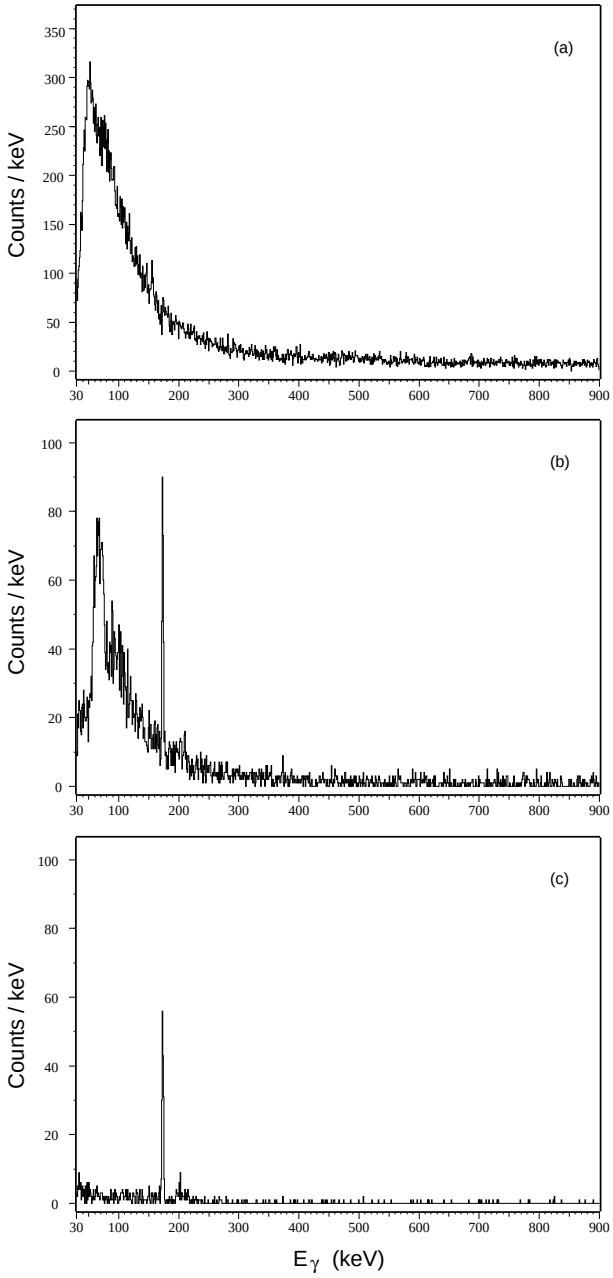

Figure 4.7: Gamma-ray spectra recorded in all four Ge-detectors during the ^{134}Sn production run from the ^{238}U fission experiment. All events collected in the detectors are plotted in (a). The background is strongly reduced in (b) by tagging on a selected heavy ion – ^{136}Sb in this case. The prompt burst of low energy bremsstrahlung and X-rays is suppressed by requiring events in delayed coincidence with the heavy-ion.

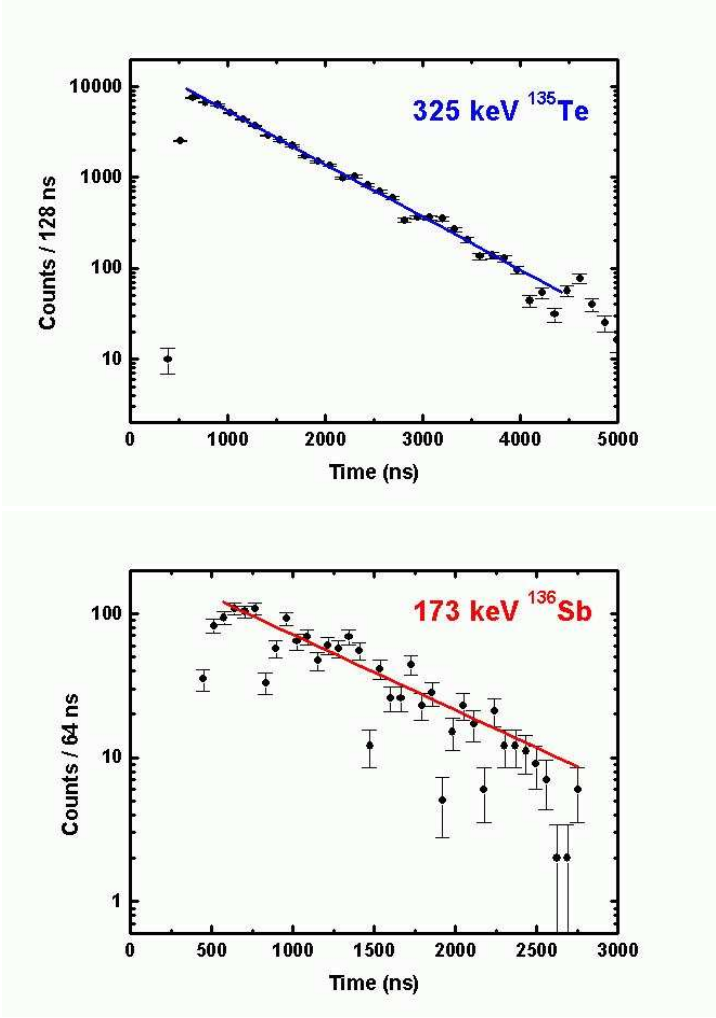

Figure 4.8: Time distribution curves of the (a) 325 keV line from the decay of the well-known $I^{\pi} = 19/2^{-}$ isomer in ^{135}Te, and (b) the 173 keV line identified in ^{136}Sb. The prompt part of the time distribution has been subtracted.

4.4 Results

4.4.1 The ^{238}U fission experiment

In the ^{238}U fission experiment we covered three production settings, optimized for ^{131}Sn, ^{134}Sn and ^{130}Cd. The first setting was aimed for calibration of the particle identification. During this experiment we observed some 35 isotopes in the neutron-rich Ag to Te isotopes with neutron numbers varying from 76 to 88. One new isomer was observed in ^{136}Sb (Paper III). In fact it was the first observation of an excited state in this isotope, which makes it the most neutron-rich Sb isotope from which γ-rays have been observed so far. In the last, most exotic setting, ^{136}Sn and ^{130}Cd were identified with about 1200 and 700 ions implanted in the aluminum

catcher, respectively. No delayed γ-rays could yet be associated with these nuclei. In addition, we have an indication for the observation of several new isotopes. The analysis of the data is still in progress. One important question which is still to be investigated is the population of isomeric states in the projectile fission reaction.

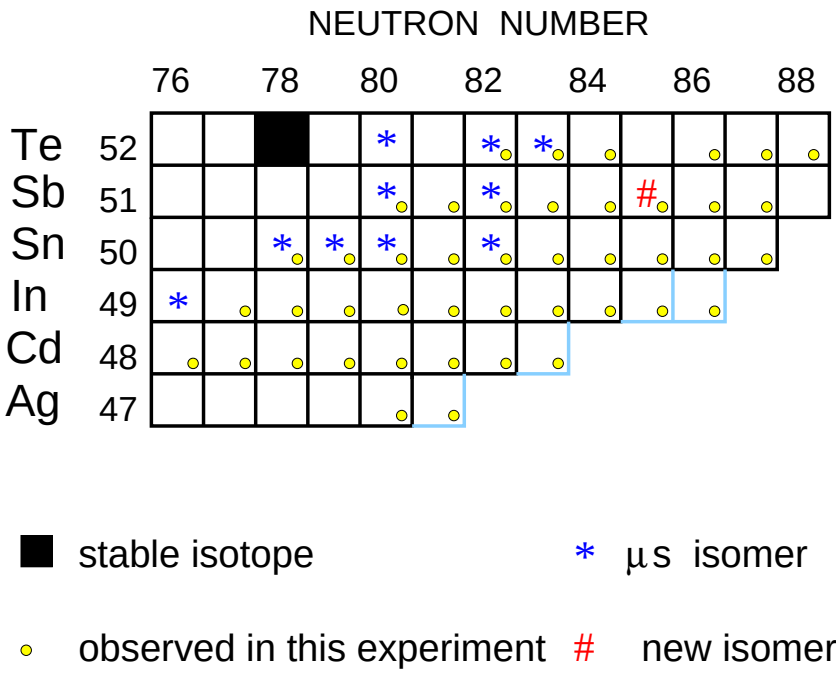

Figure 4.9: Part of the nuclidic chart showing the region covered in the ^{238}U fission experiment. All known μs isomers in the region, all isotopes and new isomers observed in this experiment are shown on the plot. For all the Cd and Ag isotopes in the plot, only the ground state has been observed so far. The grey squares represent candidates for isotopes potentially observed for the first time.

4.4.2 The ^{208}Pb fragmentation experiment

The results from the neutron-rich K-isomer search experiment are summarized in Figure 4.10. During this experiment several production settings were investigated and many neutron-rich isotopes were identified varying from Tb (Z=65) to Hg (Z=80), with neutron numbers ranging between 100 and 126. There was one setting on the proton-rich side as well, centered around $^{140}_{66}$Dy. A number of known and new isomers with lifetimes from nanosecond to millisecond ranges were observed, e.g. the $K^{\pi} = 35/2^{-}$ isomers in ^{179}W [34], ^{175}Hf [35], and ^{181}Re [36]. This is the highest angular momentum observed to be populated in projectile fragmentation so far. The shortest lifetime measured in this experiment, belonging to the $K^{\pi} = 7^{-}$ isomer in ^{200}Pt, was 14 ns [37]. This time is much shorter than the flight time trough the separator. Our explanation is that this is due to the primary transition energy

being less than the K-shell binding energy in platinum (78 keV). Thus the decay can only occur via electron conversion. Hence it is only when the ion is implanted in the catcher that the isomeric state can be depopulated and attain its natural half-life. A number of new isomers were discovered in this experiment and are indicated in Figure 4.10. Some new and very neutron-rich isotopes were also identified including ^{187,188}Ta, ^{191}W, ^{193,194}Re (see Paper I and Ref. [37, 38]), confirming the work of Reference [39].

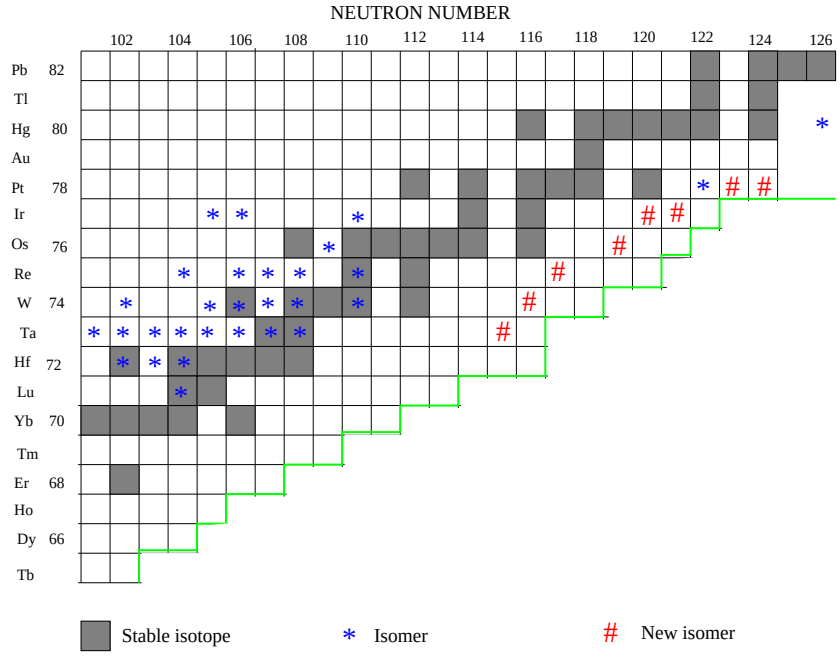

Figure 4.10: Part of the nuclidic chart showing the region which has been covered in the ^{208}Pb fragmentation experiment. The isomers known from before and observed also in our experiment are marked as well as the new isomers which have been observed for the first time in this experiment.

4.5 Isomeric ratio

The *isomeric ratio* R is by definition the ratio between the number of ions which have been produced in an isomeric state, to the total number of ions created in the reaction per given species. It is the probability that in the reaction a nucleus is produced in an isomeric state. The population probability of μs isomer in either projectile fragmentation or in-flight fission is of great importance from a reaction mechanism study point of view. The knowledge of this ratio and its dependence on the spin and excitation energy of the isomer, will make planning of future experiments more expedient and realistic. The ratio R can be determined in the following

way:

$$R = \frac{N^{isom}(t{=}0)}{N^{tot}(t{=}0)} \ , \tag{4.5.1}$$

The schematic plot in Fig. 4.11 helps to understand the determination procedure.

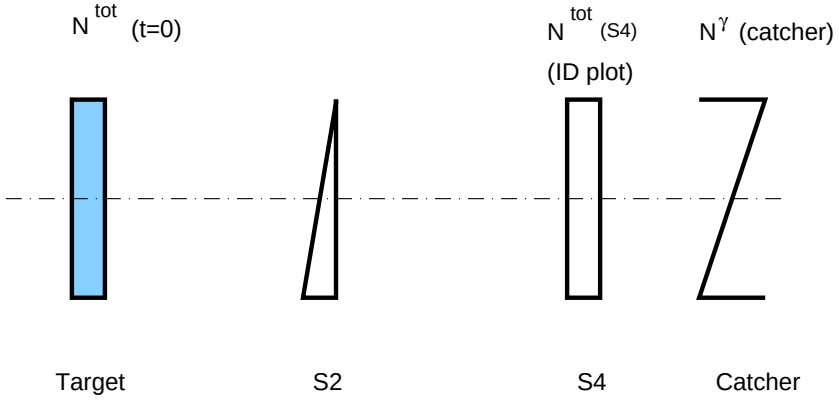

Figure 4.11: Schematic plot of the FRS.

The total number of nuclei produced in the reaction, N^{tot}, and the number of nuclei produced in an isomeric state, N^{isom}, can be determined from the experimental data we measure at the final focal plane S4, if we take in account the transmission T from the target to S4.

$$N^{tot}(S4) = N^{tot}(t=0)T_{(target-S4)} \ , \tag{4.5.2}$$

$$N^{isom}(S4) = N^{isom}(t=0)T_{(target-S4)}F \ , \tag{4.5.3}$$

where F takes into account the in-flight decay.

From (4.5.1), (4.5.2) and (4.5.3) we determine

$$R = \frac{N^{isom}(S4)}{T_{(target-S4)}F}\frac{T_{(target-S4)}}{N^{tot}(S4)} = \frac{N^{isom}(S4)}{FN^{tot}(S4)} \ , \tag{4.5.4}$$

The total number of ions at S4, $N^{tot}(S4)$, we determine from the identification (ID) plot. The ions in an isomeric state we can determine from the number of detected γ-rays N^{γ} at the catcher

$$N^{\gamma}(catcher) = N^{isom}(catcher)G\varepsilon_{\gamma}b_{\gamma}P_{\gamma} \ , \tag{4.5.5}$$

where ε_{γ} is the absolute efficiency for detecting γ-rays of energy ε_{γ}, P_{γ} is the correction factor for effective efficiency, which takes in account the blocking of the detectors during the low energy prompt flash, b_{γ} is the branching ratio for γ transitions. G is a correction for the finite time window selected in the analysis procedure

when extracting delayed γ-ray spectrum for the given isomeric transition.

The number $N^{isom}(catcher)$ is different from the one we measure, and

$$N^{isom}(catcher) = N^{isom}(S4)T_{(S4-catcher)} \quad , \tag{4.5.6}$$

or

$$N^{isom}(S4) = \frac{N^{\gamma}(catcher)}{T_{(S4-catcher)}G\varepsilon_{\gamma}b_{\gamma}P_{\gamma}} \quad , \tag{4.5.7}$$

Combining (4.5.4) and (4.5.7) we obtain for the isomeric ratio R

$$R = \frac{N^{\gamma}(catcher)}{T_{(S4-catcher)}FG\varepsilon_{\gamma}b_{\gamma}P_{\gamma}N^{tot}(S4)} \quad , \tag{4.5.8}$$

The transmission $T_{(S4-catcher)}$ can be estimated from the MOCADI code [27]. The factor F is calculated from

$$F = exp[-\sum_i(\frac{ln2\,(TOF)_i}{\gamma_i T_{1/2}^{q_i}})] \quad , \tag{4.5.9}$$

where i=1 to 4 are the four stages of the FRS, $T_{1/2}^{q_i}$ are the half-lives of the ion in the corresponding charge state, and γ is the Lorentz factor.

The correction factor G is calculated from:

$$G = exp[-\frac{ln2\,t_0}{T_{1/2}}][1 - exp[-\frac{ln2\,\Delta t}{T_{1/2}}]] \quad , \tag{4.5.10}$$

where t_0 and Δt are the start of the γ-ray detection and the time window in which data were collected, respectively.

The determination of the isomeric ratio is a very complicated procedure, which requires an absolute efficiency calibration. This is not an easy task considering the geometry of the Ge detector set-up and the large size of the beam spot. For this purpose we have measured calibration spectra with standard sources placed at ten different geometrical points in the x–direction at the catcher. The analysis of the isomeric ratios of the ^{208}Pb fragmentation experiment was completed recently and the results will be submitted for publication [31]. The analysis of isomeric ratios from the ^{238}U fission experiment is still in progress.

The experimental results can be compared with isomeric ratios predicted by theoretical models. The abrasion-ablation model has been applied [40] to describe the distribution of angular momenta populated in projectile fragmentation reactions. Using the model distributions the isomeric ratio can be calculated under the extreme simplifying assumption that R is equal to the probability that the final reaction product is produced with an angular momentum larger than that of the isomer. Results of such a comparison are available in Ref. [41], where the experimental isomeric ratios of neutron-rich isotopes in the Pb region produced by projectile fragmentation of ^{238}U are shown to be in very good agreement with the ones predicted by the model. For the in-flight fission reaction, the fragment angular momentum distribution populated in the reaction is still under investigation.

Chapter 5

Discussion

5.1 Neutron-rich antimony isotopes

Figure 5.1 shows the neutron and proton single-particle levels around the $N = 82$ and $Z = 50$ closures. The lowest excitations for the nuclei having few valence particles or holes above or below the closures will be determined by the orbitals available for these valence particles (holes).

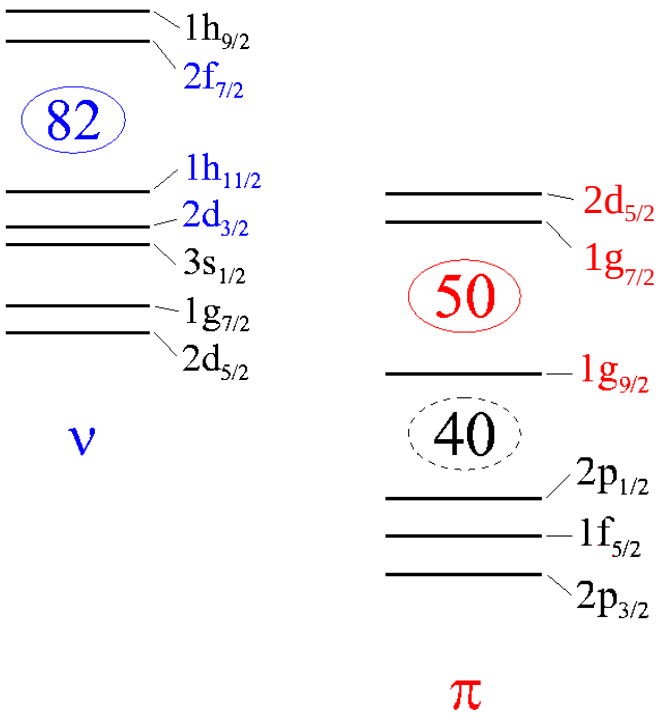

Figure 5.1: Single-particle orbitals for neutrons (ν) and protons (π) around the $N = 82$ and $Z = 50$ closures.

In nuclei around ^{132}Sn the coupling of the valence particles and holes occupying

relatively high-j orbitals often gives rise to low-spin isomers. One example is the isomer newly identified in ^{136}Sb reported in Paper III.

The stiffness of the ^{132}Sn doubly-magic core promises that the single-particle states in the surrounding nuclei should be rather pure. In Paper III we investigate the development of the shell structure comparing the two valence particle nucleus ^{134}Sb (one proton and one neutron above the doubly-magic core) with the isotope ^{136}Sb, which has four valence particles. The development of collectivity and the role of high-j orbitals is discussed when adding a pair of neutrons. We performed shell model calculations for both ^{134}Sb and ^{136}Sb, using two different approaches - namely, the Kuo-Herling shell model (KHSM), and an empirical shell model (ESM). Two sets of interactions have been used to calculate the excitation energies for the lowest multiplets - $\pi g_{7/2}\nu f_{7/2}$ in ^{134}Sb, and $\pi g_{7/2}\nu f^3_{7/2}$ in the case of ^{136}Sb.

The results of the calculations are plotted in Figures 4 and 5 in Paper III. The KHSM model uses realistic two-body matrix-elements from the ^{208}Pb region but scaled down by $A^{-1/3}$ in the full $Z = 50$ to 82 and $N = 82$ to 126 model space with mixing. The empirical shell-model uses two-body matrix-elements from ^{210}Bi, scaled from the $\pi h_{9/2}\nu g_{9/2}$ multiplet to the $\pi g_{7/2}\nu f_{7/2}$ multiplet, and $f^2_{7/2}$ two-body matrix-elements from ^{134}Sn. Pure configurations are assumed. Surprisingly, the KHSM and ESM calculations agree almost perfectly, both for ^{134}Sb and for ^{136}Sb. Therefore, including of mixing (KHSM), does not affect strongly the calculations. This means that if there were other orbitals involved in the lowest excitations in those two nuclei, their contribution should be very small, i.e., the configurations are rather pure. The agreement with the experimental data is very good in the case of ^{134}Sb. Since we observe only one γ-ray transition from ^{136}Sb it is difficult to compare the data with the calculations, but the ground state of $I^\pi = 1^-$ predicted by both calculations is in agreement with the ground state spin and parity deduced experimentally by Hoff *et al.* [42].

On the other side, the distribution of the level excitation energy as a function of angular momentum in the lowest multiplets looks very different for the two nuclei. While for ^{134}Sb the lowest and the highest spin members of the multiplet are lower in excitation energy relative to most of the levels in between, the corresponding states are located higher in ^{136}Sb and the level distribution is nearly flat. This 'parabola', which flattens from ^{134}Sb to its neighbour ^{136}Sb, reminds very much on the behaviour of the lowest multiplets in the corresponding counterparts in the ^{208}Pb region, ^{210}Bi and ^{212}Bi, discussed by Alexa *et al.* [43]. The authors study the reverse of the energy versus spin parabola as one goes from ^{210}Bi by adding pairs of neutrons and/or protons to ^{212}Bi, ^{212}At, ^{216}At, ^{216}Fr. With and without mixing they calculate the sequence of shell-model configurations in these odd-odd nuclei. The calculations without mixing show that the parabolic structure reverses as one goes from particle-particle configurations to particle-hole or hole-particle configurations. We expect that in the neighbouring odd-odd antimony isotopes with larger neutron excess, with the increasing occupation of the neutron $f_{7/2}$ orbital, the particle-particle proton-neutron interaction in ^{134}Sb will change into a particle-hole interaction in ^{140}Sb, which will invert the parabola distribution via the rather flat distribution calculated for ^{136}Sb.

5.2 K-isomers in the A =180-200 mass region

In the $A \approx$180 mass region the nuclei are deformed and axially symmetric. Therefore, they are good rotors, i.e. they show collective rotational bands with excitation energies proportional to $I(I+1)$. The isomeric state is normally the band head of a rotational band and the isomer decays to a band with lower K. Since many valence particles contribute to the configuration of the K-isomeric state, it is difficult to perform shell-model calculations in an appropriate model space to explain the excitations in such nuclei.

For example, in the case of the newly observed γ-ray cascade in ^{190}W (see Fig. 2 in Paper I) we have performed blocked BCS (Bardeen–Cooper–Schrieffer) calculations in the way described in Ref. [17]. The quasi-particle energies and the strength of the pairing force were fitted to known states in the neighbouring ^{190,191,192}Os and ^{191}Re nuclei. The calculations suggest a low-lying two-quasiparticle state with $K^\pi = 10^-$ and a $\nu[505]9/2^- \otimes \nu[615]11/2^+$ Nilsson configuration.

An isomer with the same structure has been suggested in the $N = 116$ isotone ^{192}Os. The $N = 116$ isotones ^{192}Os and ^{194}Pt are well known examples of γ-soft nuclei [44, 45]. In a simple model, the ratio of the excitation energies of the first 4^+ and 2^+ states can be used to distinguish between an axially symmetric deformed rotor (for which the ratio is 3.33), a spherical, vibrational nucleus (the ratio is 2.0), and a γ-soft nucleus ($\approx$ 2.5). The deduced ratio of the energies of the 4^+ and 2^+ in ^{190}W is 2.72, which is close to the asymptotic limit of 2.5 for a γ-soft nucleus [46, 47].

We have also performed configuration-constrained potential-energy-surface calculations, according to the mechanism of Ref. [48], for the $K^\pi = 10^-$ state in ^{190}W. The results, plotted in Fig. 4, Paper I, predict almost identical shapes for the isomeric state and the ground state, and suggest significant γ-softness, which is in agreement with the conclusion from the $4^+/2^+$ energy ratio.

Further examination of the ratio of the 4^+ and 2^+ energies in comparison with several even-even nuclei in the neighbourhood was done as illustrated in Fig. 5 in Paper I. The experimental data point for ^{190}W deviates strongly from the general trend. While the energies of the first two excited states of ^{190}W can be explained in terms of triaxiality, their ratio compared to the systematics is not fully understood. The question could be related to a breakdown of the $Z = 64$ shell gap for $N < 78$ and $N > 88$ [47, 49], and to the possibility of a sub-shell gap for proton number 76 proposed by Mach [50] in a discussion of the alteration of effective shell gaps in this neutron-rich region.

It should, however, be noted that the discussion above is based on the level scheme presented in Fig. 3, Paper I. The scheme was constructed on the basis of γ-ray singles information (the statistics did not allow a $\gamma\gamma$ coincidence analysis) and comparisons with neighbouring nuclei. It is therefore possible that the level ordering could be different.

Chapter 6

Conclusions

Projectile fragmentation and in-flight fission of relativistic heavy ions are highly successful mechanisms for producing secondary radioactive nuclear beams of exotic nuclei. The combination of a fragment separator with a germanium detector array mounted at the final focal plane of the spectrometer is a powerful tool for spectroscopy studies of nuclear systems at the limits. The separator allows for in-flight event-by-event identification of selected exotic ions. In this way previously inaccessible areas of the nuclidic chart have been opened up for γ-ray spectroscopy. In two experiments performed at the Fragment Separator at GSI, Darmstadt, using this technique, we searched for isomeric states around the doubly-magic nucleus ^{132}Sn, and in the neutron-rich Hf/W/Os isotopes. We have found a number of new isomers extending the experimental knowledge towards the neutron-rich side of the nuclidic chart. Still many questions remain open and from the spectroscopic information obtained for neutron-rich neighbours of ^{132}Sn, as well as in the Hf/W/Os region it is clear that further studies of the evolution of low-lying single-particle and collective excitations as a function of the neutron number is needed.

The information from a purely technical point of view provided from these experiments and the experience gained in the course of them is also an important issue, which is very helpful in the process of designing and the development of new radioactive nuclear beam facilities.

Acknowledgements

I would like to thank all my colleagues in the Nuclear Structure Group for the very nice physics discussions during the regular group meetings we have had.

In particular I would like to express my sincere gratitude to Prof. Claes Fahlander for giving me the opportunity to join the group, and in this way giving me the chance to see, and work with the most modern and advanced experimental nuclear physics facilities, for frequently suggesting me and my fellow students from the group to report the stage of our work, and for always asking questions in a way that inspires deeper insight and understanding of physics.

Especially I would like to thank my supervisor Dr. Margareta Hellström for the unremitting work to explain and help me understand the details of the experimental techniques, for the nice time spent working together, and for letting me think before giving me the next task.

I am very grateful to Dr. Dirk Rudolph for the help and the friendly support I get, and for giving a nice rhythm to my work.

The discussions we have had with the Mathematical Physics group held in the nice atmosphere of coffee and cookies proved once again that physics can be fun when relaxed environment is present.

In addition, I would like to thank all the collaborators from the "GSI Isomer Collaboration" for the friendly team work and nice atmosphere during the experiments.

But most of all, I want to express my thankfulness to my family, for understanding me in my aspiration to explore the so abstract to them phenomena of the nuclear structure, and my husband, Nikolay, for the discussions in the light of other fields of physics. I want to thank them for their unconditioned support and love.

References

[1] J. Blomqvist, *Proc. of the 4th International Conference on Nuclei Far From Stability*, Helsingör 1981, (Report No. 81-09, CERN, Geneva, 1981), p. 536

[2] G.A. Leander, J. Dudek, W. Nazarewicz, J.R. Nix, and Ph. Quentin, Phys. Rev. C **30**, (1984) 416.

[3] J.P. Omtvedt, H. Mach, B. Fogelberg, D. Jerrestam, M. Hellström, L. Spanier, K.I. Erokhina, and V.I. Isakov, Phys. Rev. Lett. **75**, (1995) 3090.

[4] M. Bernas *et al.*, Phys. Lett. B **331**, (1994) 19.

[5] R. Grzywacz *et al.*, Phys. Rev. C **55**, (1997) 1126

[6] W. Nazarewicz, JYFL Summer School, Jyväskylä, Finland, 1999

[7] J. Dobaczewski, I. Hamamoto, W. Nazarewicz, and J.A. Sheikh, Phys. Rev. Lett. **72**, (1994) 981.

[8] T. Werner *et al.*, Z. Phys. A **358**, (1997) 169.

[9] J. Dobaczewski, W. Nazarewicz, and T.R. Werner, Phys. Scr. T **56**, (1995) 15.

[10] J. Dobaczewski, W. Nazarewicz, T.R. Werner, J.F. Berger, C.R. Chinn, and J. Dechargé, Phys. Rev. C **53**, (1996) 2809.

[11] J.P. Omtvedt, Ph.D. thesis, University of Oslo (1995).

[12] B. Fogelberg *et al.*, Phys. Rev. Lett. B **73**, (1994) 2413.

[13] H. Grawe and M. Lewitowicz, submitted to Nucl. Phys. A.

[14] K.E. G. Löbner, *et al.*, Phys. Lett. B **26**, (1968) 369.

[15] P.M. Walker and G.D. Dracoulis, submitted to Hyperfine Interactions.

[16] S. Åberg, Nucl. Phys. A **306**, (1978) 89.

[17] K. Jain, *et al.*, Nucl. Phys. A **591**, (1995) 61.

[18] N. Bohr and F. Kalckar, Det Kgl. Danske Videnskabernes Selskab, Mathematisk-fysiske Meddelelser **XIV**, 10, København, Levin and Munksgaard, 1937.

[19] R. Pfaff, Ph.D. thesis, Michigan State University (1996).

[20] R. Serber, Phys. Rev. **72**, (1947) 1114.

[21] P. Armbruster *et al.*, Z. Phys. A **355**, (1996) 191.

[22] Ch.O. Engelmann, Ph. D. thesis, Universität Tübingen, DISS.98-15, July 1998.

[23] H. Geissel *et al.*, Nucl. Instr. Meth. B **70**, (1992) 286.

[24] C. Ziegler *et al.*, Sci. Rep. GSI-91-1, (1991) p.291.

[25] M. Steiner, Diplomarbeit, TH Darmstadt (1991).

[26] J. Simpson *et al.*, Heavy Ion Phys. Res. II, (2000) p. 159

[27] N. Iwasa, H. Geissel, G. Münzenberg, C. Scheidenberger, Th. Schwab, and H. Wollnik, Nucl. Instr. Meth. B **126**, (1997) 284.

[28] C. Scheidenberger and H. Geissel, Nucl. Instr. Meth. B **135**, (1998) 25.

[29] M. Pfützner, B. Voss, H.-G. Clerc, H. Geissel, G. Münzenberg, F. Nickel, K.-H. Schmidt, M. Steiner, K. Sümmerer, and D.J. Vieira, Sci. Rep. GSI-91-1, (1991) p. 288.

[30] C. Scheidenberger, Th. Stöhlker, W.E. Meyerhof, H. Geissel, P.H. Mokler, and B. Blank, Nucl. Instr. Meth. B **142**, (1998) 441.

[31] M. Pfützner *et al.*, Phys. Rev. C, to be submitted

[32] http://www-aix.gsi.de/∼wolle/EB_at_GSI/main.html

[33] J. Kantele, "Handbook of nuclear spectrometry", Academic Press, Harcourt Brace and Company 1995.

[34] P.M. Walker *et al.*, Nucl. Phys. A **568**, (1994) 397.

[35] G.D. Dracoulis and P.M. Walker, Nucl. Phys. A **342**, (1980) 335.

[36] C.J. Pearson *et al.*, Phys. Rev. Lett. **79**, (1997) 605.

[37] M. Caamaño *et al.*, Acta. Phys. Pol. B **32**, (2001) 763.

[38] Ch. Schlegel *et al.*, Physica Scripta T **88**, (2000) 72.

[39] J. Benlliure *et al.*, Nucl. Phys. A **660**, (1999) 87.

[40] M. de Jong *et al.*, Nucl. Phys. A **613**, (1997) 435.

[41] M. Pfützner *et al.*, Phys. Rev. B **444**, (1998) 32.

[42] P. Hoff, J.P. Omtvedt, B. Fogelberg, H. Mach, and M. Hellström, Phys. Rev. C **56**, (1997) 2865

[43] P. Alexa and R. Sheline, Phys. Rev. C **56**, (1997) 3087.

[44] C.Y. Wu *et al.*, Nucl. Phys. A **607**, (1996) 178.

[45] C. Wheldon *et al.*, Nucl. Phys. A **652**, (1999) 103.

[46] R.F. Casten, "Nuclear Structure from a Simple Perspective", Oxford University Press, Oxford 1990.

[47] R.F. Casten, *et al.*, Phys. Rev. Lett. **47**, (1981) 1433.

[48] F. Xu *et al.*, Phys. Lett. B **435**, (1998) 257.

[49] J.A. Cizewski and E. Gülmez, Phys. Lett. B **175**, (1986) 11.

[50] H. Mach, Phys. Lett. B **185**, (1987) 20.